1 **[Article Full Title]**

2 A Dual-supervised Deformation Estimation Model (DDEM) for Constructing Ultra-quality

3 4D-MRI based on a Commercial Low-quality 4D-MRI for Liver Cancer Radiation Therapy

4 **[Short Running Title]**

5 DDEM for Ultra-quality 4D-MRI

6 **[Author Names]**

7 Haonan Xiao[1], Ruiyan Ni[1], Shaohua Zhi[1], Wen Li[1], Chenyang Liu[1], Ge Ren[1], Xinzhi Teng[1],

8 Weiwei Liu[2], Weihu Wang[2], Yibao Zhang[2], Hao Wu[2], Ho-Fun Victor Lee[3], Lai-Yin Andy

9 Cheung[4], Hing-Chiu Charles Chang[5], Tian Li[1], Jing Cai[1]

10 **[Author Institutions]**

11 [1] Department of Health Technology and Informatics, The Hong Kong Polytechnic University,

12 Hong Kong SAR, China

13 [2] Key Laboratory of Carcinogenesis and Translational Research (Ministry of

14 Education/Beijing), Department of Radiation Oncology, Beijing Cancer Hospital & Institute,

15 Peking University Cancer Hospital & Institute, Beijing, China

16 [3] Department of Clinical Oncology, The University of Hong Kong, Hong Kong SAR, China

17 [4] Department of Clinical Oncology, Queen Mary Hospital, Hong Kong SAR, China

18 [5] Department of Radiology, The University of Hong Kong, Hong Kong SAR, China

19 **[Corresponding Author Name & Email Address]**

20 Jing Cai, jing.cai@polyu.edu.hk, corresponding author

21 Tian Li, litian.li@polyu.edu.hk, co-corresponding author

22 **[Author Responsible for Statistical Analysis Name & Email Address]**

23 Haonan Xiao, haonan.xiao@connect.polyu.hk

24 **[Conflict of Interest Statement for All Authors]**

34 **[Data Availability Statement for this Work]**

35 Research data are not available at this time.

36 **[Acknowledgements]**

37

Abstract

Background: Most available 4D-MRI techniques are limited by insufficient image quality and long acquisition times or require specially designed sequences or hardware that are not available in the clinic. These limitations have greatly hindered the clinical implementation of 4D-MRI.

Purpose: This study aims to develop a fast ultra-quality (UQ) 4D-MRI reconstruction method using a commercially available 4D-MRI sequence and dual-supervised deformation estimation model (DDEM).

Methods: Thirty-nine patients receiving radiotherapy for liver tumors were included. Each patient was scanned using a TWIST-VIBE MRI sequence to acquire 4D-MR images. They also received 3D T1-/T2-weighted MRI scans as prior images and UQ 4D-MRI at any instant was considered a deformation of them. A DDEM was developed to obtain a 4D deformable vector field (DVF) from 4D-MRI data, and the prior images were deformed using this 4D-DVF to generate UQ 4D-MR images. The registration accuracies of the DDEM, VoxelMorph (normalized cross-correlation (NCC) supervised), VoxelMorph (end-to-end point error (EPE) supervised), and the parametric total variation (pTV) algorithm were compared. Tumor motion on UQ 4D-MRI was evaluated quantitatively using region-of-interest (ROI) tracking errors, while image quality was evaluated using the contrast-to-noise ratio (CNR), lung–liver edge sharpness, and perceptual blur metric (PBM).

Results: The registration accuracy of the DDEM was significantly better than those of VoxelMorph (NCC supervised), VoxelMorph (EPE supervised) and the pTV algorithm

60   (all, $p < 0.001$), with an inference time of 69.3 ± 5.9 ms. UQ 4D-MRI yielded ROI

61   tracking errors of 0.79 ± 0.65, 0.50 ± 0.55, and 0.51 ± 0.58 mm in the superior–inferior,

62   anterior–posterior, and mid–lateral directions, respectively. From the original 4D-MRI

63   to UQ 4D-MRI, the CNR increased from 7.25 ± 4.89 to 18.86 ± 15.81; the lung–liver

64   edge full-width-at-half-maximum decreased from 8.22 ± 3.17 to 3.65 ± 1.66 mm in the

65   in-plane direction and from 8.79 ± 2.78 to 5.04 ± 1.67 mm in the cross-plane direction,

66   and the PBM decreased from 0.68 ± 0.07 to 0.38 ± 0.01.

67   **Conclusion:** This novel DDEM method successfully generated UQ 4D-MR images

68   based on a commercial 4D-MRI sequence. It shows great promise for improving liver

69   tumor motion management during radiation therapy.

1. Introduction

Primary liver cancer and the metastasis of other cancers to the liver are leading causes of cancer-related death worldwide. Liver cancer accounted for 4.7% (905,677) of new cases and 8.3% (830,130) of deaths from all cancers in 2020[1]. Radiation therapy (RT) is a major treatment modality for cancer. Historically, however, the role of RT in liver cancer has been limited to mostly palliative applications due to the potential for radiation-induced liver disease (RILD)[2]. The recent introduction of stereotactic body radiation therapy (SBRT) for liver cancer treatment[3], however, has led to local tumor control rates of up to 86% at 3 years[4], indicating its effectiveness. Despite these exciting improvements, RT is associated with Grade $\geq$ 3 toxicity event rates as high as 38%[5], especially for patients with large tumors and poor liver function[6]. Use of an imaging modality with good soft tissue contrast during planning can help to manage tumor motion and improve the accuracy of beam delivery to the target, thus sparing normal tissues and reducing treatment toxicity.

Currently, four-dimensional computed tomography (4D-CT) is the standard imaging technique used for respiratory motion management in RT, especially when treating tumors in the chest region[7]. Unlike conventional CT, 4D-CT can show the motion trajectories of tumors during respiration; additionally, the internal target volumes (ITVs) defined on 4D-CT are significantly smaller than those on conventional CT[8, 9], while maintaining the dose coverage[10, 11]. However, management of liver tumor motion using 4D-CT is difficult due to the poor soft-tissue contrast of CT. Also, the radiation dose received by patients in 4D-CT can be up to one order of magnitude higher

4

94　than that in conventional 3D CT since multiple scans at the same couch position are

95　needed for respiratory phase sorting[12]. To address these difficulties, various 4D-MRI

96　techniques have been proposed[13] and can be categorized as either retrospective or

97　prospective 4D-MRI.

98　Most 4D-MRI techniques are retrospective, which means that images are

99　continuously acquired over the whole region of interest (ROI) and retrospectively

100　sorted into respiratory phases. For example, Yang et al. evaluated the correlation

101　between diaphragm and liver tumor motion[14, 15] and performed T2/T1-weighted 4D-

102　MRI at a speed of 10–15 s per slice using a body area-based sorting method[15]. Liu et

103　al.[16] developed a k-space re-ordering method that uses breathing signals as the surrogate

104　and verified its feasibility through studies of digital phantoms and healthy volunteers.

105　Keijnemans et al.[17] sorted images based on the liver dome position and achieved a total

106　image acquisition time of 5 minutes. Other types of contrasts, including T2-weighted

107　(T2w) imaging[18], diffusion-weighted imaging (DWI)[19], and quantitative magnetic

108　resonance fingerprinting (MRF)[20], can also be obtained via similar approaches. Despite

109　these successes, retrospective 4D-MRI still faces challenges. First, sorting algorithms

110　are sensitive to patients' irregular breathing patterns, resulting in image artifacts, such

111　as stitching artifacts. Second, the spatiotemporal resolution is compromised, especially

112　with respect to large slice thicknesses (>5 mm) obtained with 2D acquisition-based

113　methods. Third, long acquisition times (typically 10–15 minutes) are typically needed

114　to satisfy the data sufficiency requirement in each phase bin.

115　Prospective 4D-MRI is achieved by using fast 3D acquisition or respiratory-gated

116 2D acquisition. For example, Yuan et al. [21] used a 3D spoiled gradient-echo sequence

117 to image the abdomen for motion monitoring, with a temporal resolution of 0.615 s and

118 voxel size of 2.7 mm × 2.7 mm × 4 mm. Due to the emphasis on imaging speed,

119 prospective methods mainly use gradient-echo sequences and provide T1w images and

120 are thus susceptible to field inhomogeneity. As the image quality and contrast are also

121 compromised by the highly undersampled data, these images cannot be used for

122 treatment planning. Using respiratory surrogates, Li et al. [22] proposed a prospective

123 T2w 4D-MRI method involving 2D acquisition. Although the authors overcame the

124 issue of data incompetency in sorting, scanning was time-consuming (~10 minutes),

125 and the effects of irregular respiration on image quality were not resolved.

126 Despite recent advances in 4D-MRI development, current techniques still lack

127 sufficient and consistent image quality for use in clinical applications due to at least one

128 of the following deficiencies: inconsistent tumor contrast, image artifacts caused by

129 breathing variations, and inadequate spatiotemporal resolution. In addition, some

130 advanced 4D-MRI techniques require specially designed sequences or hardware and

131 advanced image reconstruction methods that are not available in the clinic. These

132 limitations have greatly hindered the clinical implementation of 4D-MRI.

133 This study aims to overcome the aforementioned deficiencies of existing 4D-MRI

134 techniques by developing a ultra-quality (UQ) 4D-MRI method that uses a novel dual-

135 supervised deformation estimation model (DDEM) based on a commercially available

136 low-quality (LQ) 4D-MRI sequence. Specifically, respiratory motion patterns in LQ

137 4D-MRI were estimated using the DDEM and then applied to pre-aligned 3D-MRI data

138   to reconstruct UQ 4D-MR images. We successfully generated T1w and T2w UQ 4D-

139   MR images that exhibited significantly improved image quality and accurate tumor

140   motion trajectory when compared with the original LQ 4D-MR images. Therefore, this

141   new technique shows promise for wide clinical application.

2. Materials and Methods

2.1 Patient Data

The data used in this study were obtained from 39 patients undergoing RT for liver tumors. The study protocol was approved by the institutional review board. Among the 39 patients, 29 were male and 8 were female. 22 patients were diagnosed with primary liver cancer and 15 patients were diagnosed with liver metastases, and their age at diagnosis was 54.9 ± 10.9 years old.

Each patient underwent 4D-MRI using the TWIST volumetric interpolated breath-hold examination (TWIST-VIBE) MRI sequence[23], which utilized view sharing technique with 20% central region and 20% sampling density in the peripheral region; hereafter, this is referred to as "original 4D-MRI." This commercially available sequence was initially designed for fast volumetric imaging rather than 4D imaging. In this study, we decreased the acquisition time to 0.69s and continuously acquired 72 3D frames to achieve a 4D-MRI scan. Of the 39 patients, 27 also underwent regular T1w (free-breathing) and T2w (breath-holding) 3D MRI scans. Details of the imaging parameters are listed in **Table 1**. All the MR scans were done by a 3T scanner (Skyra, Siemens, Erlangen, Germany). All of the image intensities were normalized to 0-1 as pre-processing. For DDEM training, the original 4D-MR images were sorted into 10 phase bins based on the body area[15] and paired up with a phase distance of 1, 2, 3, and 4, respectively. As a results, every patient contributes 40 image pairs. Patients with a low breathing amplitude or whose data contained severe artifacts were excluded from training. Cross-validation was conducted to fully utilize the data. Consequently, 25

164 patients were divided into 5 groups, each containing 5 patients. In each time, 4 groups

165 with 800 image pairs were used for training and the remaining one with 200 image pairs

166 was used for evaluation. Image binning was not needed for UQ 4D-MRI reconstruction,

167 as deformations were directly estimated on time-resolved original 4D-MRI frames.

168

169 **Table 1:** Imaging parameters of the enrolled patients.

	Original 4D-MRI	T1w 3D MRI	T2w 3D MRI
No. of Patients	39	27	27
Contrast-enhanced	No	Yes	No
Acquisition mode	Free breathing	Free breathing	Gated
Sequence	TWIST-VIBE	Star-VIBE	TSE
Fat suppression	N/A	SPAIR	SPAIR
Turbo factor	N/A	N/A	43
Flip angle (°)	5	9	72
Echo trains per slice	N/A	N/A	6
Parallel imaging (factor)	CAIPIRINHA (4)	N/A	GRAPPA
Acceleration factor (PE)	2	N/A	3
Partial Fourier	6/8	7/8	N/A
TR (ms)	3.44	2.83	1090.0
TE (ms)	1.23/2.45	1.48	84.0
Bandwidth (Hz/pixel)	1420	820	781
Matrix size	$160 \times 128 \times 64$	$320 \times 320 \times 72$	$256 \times 256 \times 40$
Voxel size (mm)	$2.7 \times 2.7 \times 2.7$	$1.2 \times 1.2 \times 3.0$	$1.5 \times 1.5 \times 5.0$
Acquisition time	0.69 s per 3D frame	173 s	60 s
No. of frames	72	N/A	N/A

170 3D: Three-dimensional; 4D: Four-dimensional; CAIPIRINHA: Controlled aliasing in

171 parallel imaging results in higher acceleration; GRAPPA: Generalized autocalibrating

172 partial parallel acquisition; MRI: Magnetic resonance imaging; SPAIR: Spectral

173 attenuated inversion recovery; T1w: T1-weighted; T2w: T2-weighted; TE: Echo time;

174 TR: Repetition time; TSE: Turbo spin echo; TWIST: time-resolved imaging with

175 interleaved stochastic trajectories; VIBE: volumetric interpolated breath-hold

176 examination.

177
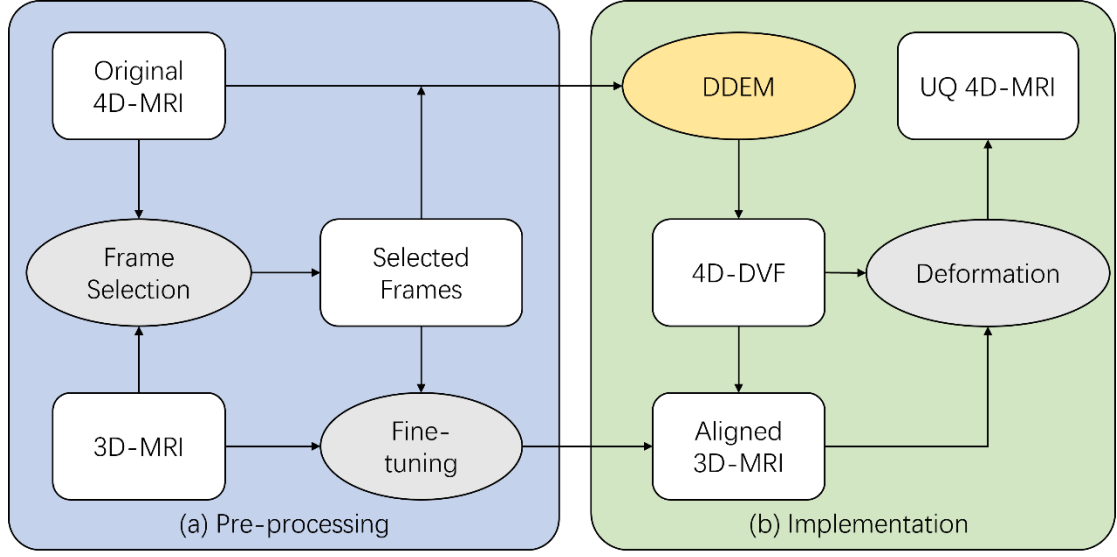
Figure 1: The overall study design of the proposed UQ 4D-MRI technique. (a) The original 4D-MRI frames whose respiratory phases were closest to that of the 3D-MR images were selected, and Elastix was used to fine-tune the residual mismatching. (b) A 4D-DVF between the selected frames and other frames was obtained via DDEM and applied to the aligned 3D-MR image to reconstruct the UQ 4D-MR images using corresponding frames. 4D: four-dimensional; DDEM: dual-supervised deformation estimation model; MRI: magnetic resonance imaging; DVF: displacement vector field UQ: ultra-quality.

2.2 UQ 4D-MRI Reconstruction

The retrospective 4D-MRI method provides good spatial resolution and image contrast, while the prospective 4D-MRI method provides fine temporal resolution with few irregular breathing-induced artifacts. To combine the advantages of both methods, a prior image-based UQ 4D-MRI method was proposed. An overview of the method is

10

193   shown in **Figure 1**. 3D MR images were deformed to each corresponding frame of the

194   original 4D-MRI to reconstruct UQ 4D-MRI. Two aspects of this approach are

195   challenging: potential differences in the respiratory phases of the 3D MR images used

196   as prior images and those of the 4D-MRI frames, and the use of deep learning for image

197   registration with several different types of image contrast[24-26]. Therefore, an automatic

198   frame selection strategy was used instead of registering 3D MR images to every original

199   4D-MRI frame. Cross-correlation was computed between all 4D-MRI frames and the

200   corresponding 3D MRI (T1w or T2w). The 4D-MRI frame of the highest cross-

201   correlation value was considered at the closest respiratory phase of the corresponding

202   3D MRI, which was then registered to the 3D MRI using Elastix (Available at

203   https://github.com/raacampbell/matlab_elastix) to account for residual mismatches.

204   The registration is hierarchical and includes rigid, affine, and non-rigid B-spline stages

205   to address coarse-to-fine deformations. Normalized correlation coefficient is the cost

206   function because of the multi-parametric MRI registration. More details can be found

207   at Mengler et al.'s work[27]. The alignment was manually verified before UQ 4D-MRI

208   reconstruction. After these pre-processing procedures, the aligned frames were

209   considered representations of the 3D MR images and registered to all other original 4D-

210   MRI frames using DDEM to obtain the deformations along with the respiratory cycles

211   (i.e., a 4D-DVF), which were then applied to the 3D MR images to reconstruct UQ 4D-

212   MR images at corresponding frames.

213

214   **2.3 DDEM**

215   The original 4D-MR images were subject to noise and artifacts due to acquisition

216   limitations, and thus, unsupervised training was challenging. Dual supervision was used

217   to provide more accurate DVFs for UQ 4D-MRI reconstruction[28]. From each original

218   4D-MR image pair, a reference DVF was calculated using the parametric total variation

219   (pTV) algorithm with the local correlation coefficient as the cost function[29]. This

220   method was designed explicitly for respiratory motion registration and has achieved the

221   best performance to date on the benchmark DIR-Lab[30, 31]. A difference map between

222   the image pair was also fed to the DDEM to improve registration accuracy[28, 32]

223   Consequently, each training sample consisted of a moving phase, a fixed phase, a

224   difference map, and a reference DVF. During training, the 4D-MR images and reference

225   DVFs were cropped to fit the patients' body shapes and resized to $128 \times 128 \times 64$ voxels

226   to save GPU memory. In addition to the end-to-end point error (EPE) between the

227   reference deformation DVF_r and the predicted deformation DVF_p, the negative

228   normalized correlation coefficient (NCC) between the warped volume V_w and fixed

229   volume V_f was also included in the loss function L to compensate for potentially

230   imperfect reference DVFs:

231    $$L = \alpha \times EPE(DVF_r, DVF_p) - \beta \times NCC(V_w, V_f) \qquad (1.1)$$

232    $$EPE(DVF_r, DVF_p) = \left\| DVF_r - DVF_p \right\|_2 \qquad (1.2)$$

233    $$NCC(V_w, V_f) = \sum_{p \in \Omega} \frac{\left(\sum_{p_i} (V_f(p_i) - \overline{V_f(p)})(V_w(p_i) - \overline{V_w(p)}) \right)^2}{\left(\sum_{p_i} (V_f(p_i) - \overline{V_f(p)}) \right)^2 \left(V_w(p_i) - \overline{V_w(p)} \right)^2}, \qquad (1.3)$$

234   where p represents a voxel in space Ω; $\overline{V(p)}$ denotes the local mean intensity around

235   p, $\overline{V(p)} = \frac{1}{W^3} \sum_{p_i} V(p_i)$; and the window size $W = 9$. α and β are weighting

236   factors and varied dynamically during training. A larger α during the initial training

can encourage convergence, and a larger β during fine-tuning at a later stage can

further optimize the registration. We empirically set $\alpha = 1$ and $\beta = 1$ during the first

150 epochs, and $\alpha = 1$ and $\beta = 5$ during the last 50 epochs.
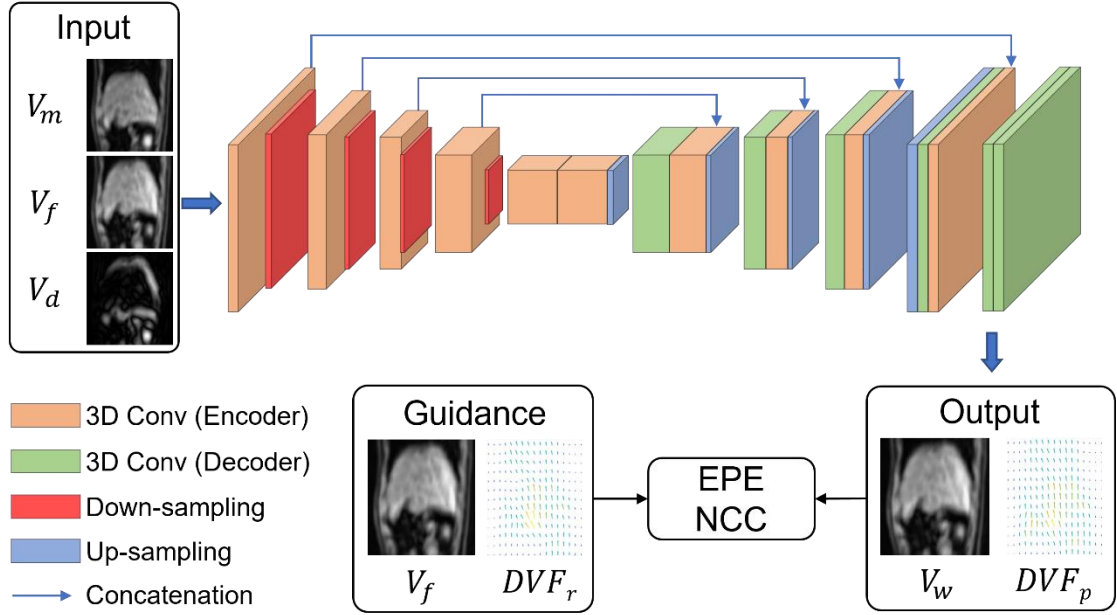
Figure 2: Architecture of the proposed DDEM. The moving volume (V_m), fixed volume

(V_f), and map of differences map between these volumes (V_d) were input to the network.

The output consisted of a predicted deformation (DVF_p) and warped volume (V_w). The

training was dually supervised by the reference deformation (DVF_r) and V_f. 3D: three-

dimensional; Conv: convolution; EPE: end-to-end point error; DVF: displacement

vector field; NCC: normalized cross correlation.

The network architecture of DDEM was based on VoxelMorph[33], as shown in

Figure 2. It receives two phases of the original 4D-MRI as moving and fixed volumes

and a difference map between them. The first half of the DDEM is an encoder consisting

of 4 sequential convolutional blocks used to extract image features. The first three

blocks have a $3 \times 3 \times 3$ convolutional layer, with a stride of 2, followed by a leaky

rectified linear unit (ReLU) activation layer, while the stride in the last one is 1. The

numbers of convolutional kernels in these blocks are 16, 32, 32, and 32, respectively.

Using the decoder, the extracted image features were then processed to generate a DVF

between the moving and fixed images. The decoder uses similar convolutional blocks

with 32 kernels each, and $2 \times 2 \times 2$ up-sampling layers are applied after each ReLU

activation to expand the feature volume. The two parts are linked by concatenation

connections, which convey local information captured by the encoder to the decoder to

better utilize the features. The last convolutional layer contains 3 convolutional kernels,

and the resulting three output channels represent motion in the x-, y-, and z-directions.

The deformation was then applied to the moving volume to generate a warped volume

V_w as another output. Another two models with the identical network architecture but

supervised by NCC and EPE were trained as comparison baselines, respectively. All

models were trained by an ADAM optimizer for 200 epochs at an initial learning rate

of 10^{-4}, which was halved every 50 epochs. Training was conducted using with

Pytorch 1.7.0 on an Nvidia RTX 3090 GPU and an Intel I7-9700K CPU.

2.4 Evaluation

The registration performances of DDEM, VoxelMorph, and pTV algorithm on the

original 4D-MRI data were evaluated using intensity-based metrics, including the

structural similarity index (SSIM), peak signal-to-noise ratio (PSNR), mean squared

274   error (MSE), and NCC. Each image was restored to its original shape prior to the metric

275   calculations. T-tests were performed on the metrics to evaluate the significance with a

276   threshold of 0.05. The inference times of the methods were also recorded for

277   comparison.

278   4D imaging is used primarily for motion management, and therefore, motion

279   accuracy is an essential component of UQ 4D-MR images. A region matching-based

280   method for ROI tracking was developed in MATLAB. 3D ROI bounding boxes were

281   defined on the first frames of 4D images and used to screen subsequent volumetric

282   frames to identify the locations with maximum image similarity in each frame. The

283   displacements between the positions of the initial bounding box and the positions in

284   subsequent frames were calculated as the ROI motion trajectory. 4D images were

285   interpolated before measurement to ensure a motion measurement resolution of 0.33

286   mm. ROI motion amplitude was recorded in the superior–inferior (SI), anterior–

287   posterior (AP), and mid–lateral (ML) directions, and the relative motion error was

288   calculated as the difference in ROI motion amplitude between the original and the UQ

289   4D-MR images.

290   The contrast-to-noise ratio (CNR) was used to quantify tumor contrast

291   enhancement in the UQ 4D MR images. Precisely, the mean voxel intensities of the

292   tumor and surrounding normal liver tissue were calculated, and the difference between

293   these values was divided by the standard deviation sampled from the normal liver tissue.

294   A no-reference perceptual blur metric (PBM) proposed by Crete et al. [34] was used

295   to evaluate the overall image quality of the original and UQ 4D MR images. Briefly,

296 PBM compares variations in the intensities of neighboring voxels between the original

297 image and an image to which a low-pass filter has been applied to cause blurring. Less

298 variation in intensity represents a more blurred original image, resulting in a higher

299 PBM value.

300 The lung–liver edge full-width at half-maximum (FWHM) was also used to

301 quantify the sharpness of the organ boundaries[35]. Linear profiles were taken at the liver–

302 lung interfaces on MR images in the cross-plane and in-plane directions, and curves

303 were fitted along with them:

304 $$f(p; a_0, a_1, a_2, s) = \frac{a_1}{1 + 10^{s(a_0 - p)}} + a_2, \tag{2}$$

305 where p is the voxel position; f is the voxel intensity at p; a_0, a_1, and a_2 are

306 fitted constants; and s represents the sharpness of the curve. Thresholds of 5% and 95%

307 of the maximum were applied to the curves to define an edge, and the distance between

308 the two thresholds was considered the FWHM of the edge.

309 Because the CNR and edge FWHM calculations involved manually selected ROIs,

310 each measurement was repeated three times, and the average value was reported. Some

311 patients had already undergone surgery before RT, and their MR images did not have

312 solid tumors. In such cases, another organ, such as the gallbladder, was chosen as a

313 substitute ROI in the motion trajectory measurement, and the CNR was not calculated.

314

315 **3. Results**

316 **3.1 Performance of the DDEM**

317 The results of a comparison of the registration performance of the DDEM,

318   VoxelMorph, and reference pTV algorithm are shown in **Table 2**. Both the DDEM and

319   VoxelMorph models had a faster inference time than the pTV algorithm. In terms of

320   image similarity, the DDEM had significantly better NCC, MSE, PSNR, and SSIM than

321   VoxelMorph (NCC supervised), VoxelMorph (EPE supervised), and pTV algorithm

322   ($p < 0.001$ for all metrics). These results suggest that dual supervision can help the

323   model to converge and surpass the reference labels.

324

325   **Table 2:** Registration results of all of the methods applied to the test set.

	MSE (10^{-3})	NCC	PSNR	SSIM	Time
w/o Registration	1.60±1.10	0.772±0.053	28.95±3.21	0.912±0.050	N/A
pTV algorithm	0.95±0.53	0.825±0.037	31.02±2.88	0.960±0.015	28.4±3.4 s
VoxelMorph (NCC supervised)	0.56±0.32	0.856±0.030	33.28±2.81	0.963±0.016	69.1±5.9 ms
VoxelMorph (EPE supervised)	1.00±0.54	0.817±0.038	30.78±2.79	0.955±0.018	69.9±5.3 ms
DDEM	0.43±0.28	0.908±0.022	34.72±3.16	0.978±0.009	69.3±5.9 ms

326   DDEM: dual-supervised deformation estimation model; MSE: Mean squared error;

327   NCC: Normalized cross-correlation; PSNR: Peak signal-to-noise ratio; pTV:

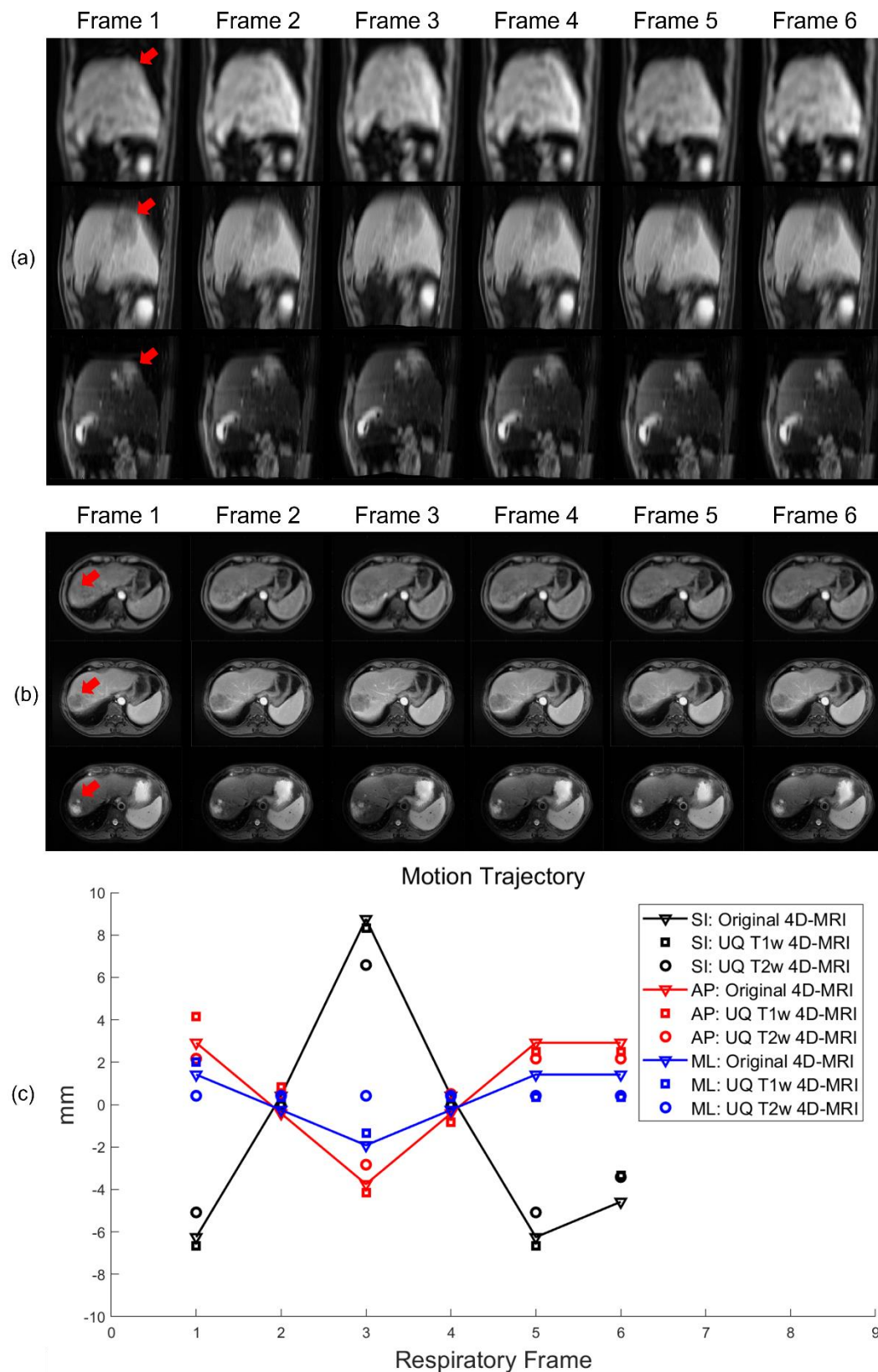328   parametric total variation; SSIM: Structure similarity index measure.

329

Figure 3: Reconstruction of an image from a sample patient using 6 consecutive frames.

(a, b) Original 4D-MR (top), UQ T1w 4D-MR (mid), and UQ T2w 4D-MR images

333 (bottom) of the patient in sagittal and axial views, respectively. Arrows indicate the

334 tumor in the first frame. The images represent 3D volumes; only 2D slices are shown

335 here for demonstration. (c) The tumor motion trajectory of this patient in the SI, AP,

336 and ML directions. UQ 4D-MR images show good matching of tumor motion with the

337 original 4D-MR data. 4D-MRI: four-dimensional magnetic resonance imaging; AP:

338 anterior-posterior; ML: mid-lateral; SI: superior-inferior; T1w: T1-weighted; T2w: T2-

339 weighted; UQ: ultra-quality.

340

341 **3.2 UQ 4D-MRI**

342   The original 4D-MR and reconstructed UQ T1w and T2w 4D-MR images of an

343 example patient in the axial and sagittal views are shown in **Figure 3(a)** and **(b)**,

344 respectively. Six consecutive frames are presented, and the arrows indicate the tumor

345 position in the first frame. As shown, the original 4D-MR images have insufficient

346 image contrast, such that the tumor is almost invisible, with a tumor CNR of only 1.9.

347 Motion artifacts can also be observed, resulting in inhomogeneous patterns in the liver

348 and blurred lung–liver boundaries. The PBM of those images was 0.700, and the

349 FWHM of the lung–liver edge was 8.92 and 12.64 mm in the cross-plane and in-plane

350 directions, respectively. In comparison, the reconstructed UQ T1w 4D-MR images

351 exhibit better tumor contrast, with a higher CNR of 7.7, and less severe motion artifacts.

352 In the reconstructed UQ T1w images, the PBM decreased to 0.426, and the FWHM of

353 the lung–liver edge decreased to 11.86 and 7.38 mm in the cross-plane and in-plane

354 directions, respectively. Additional comparison reveals that the tumor visibility was

19

further improved in the UQ T2w 4D-MR images, with the highest CNR of 14.4, a

considerable increase in lung–liver edge sharpness, and a reduction in motion artifacts.

The PBM decreased to 0.397, and the FWHM of the lung–liver edge decreased to 5.12

and 3.21 mm in the cross-plane and in-plane directions, respectively.

In addition to image quality, motion was accurately reflected in the generated UQ

4D-MR images. **Figure 3(c)** shows the motion amplitude of the tumor in 6 consecutive

frames. As expected in respiration, the motion amplitude was largest in the SI direction.

In the UQ T1w and T2w 4D-MR images, the tumor motion matched well with that in

the original 4D-MR images, and most of the relative motion errors were within 2 mm.

The respective mean motion errors in all 72 frames in the AP, ML, and SI directions

were 0.70, 0.76, and 0.62 mm for the UQ T1w 4D-MR images and 0.87, 0.90, and 0.82

mm for the UQ T2w 4D-MR images.
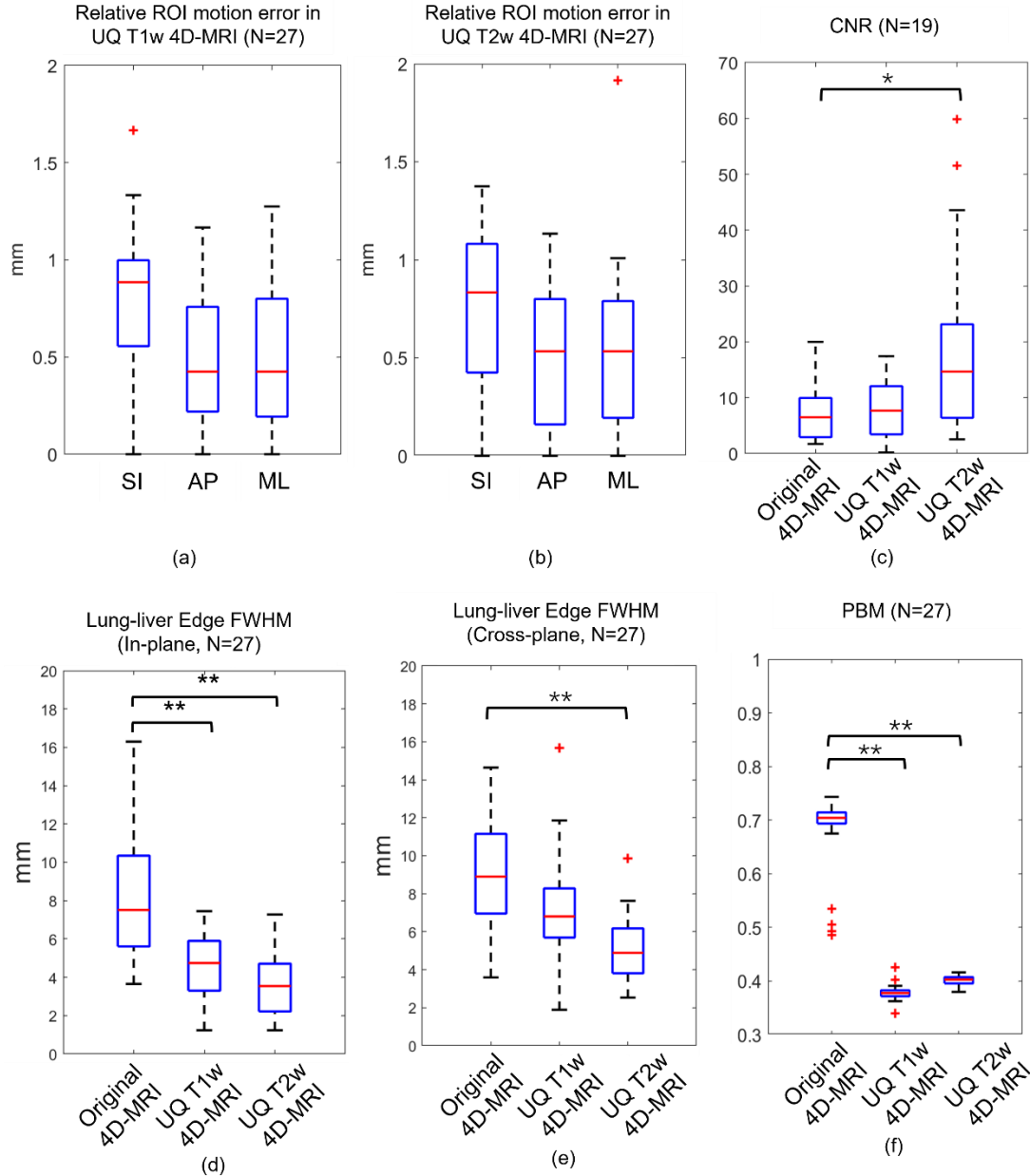
Figure 4: Statistical analysis of the patient data. (a, b) Relative ROI motion error of the UQ T1w and T2w 4D-MR images in the SI, AP, and ML directions, respectively. (c) CNR of the original 4D-MR and reconstructed UQ T1w and T2w 4D-MR images. (d, e) Lung–liver edge FWHM of the original 4D-MR and reconstructed UQ T1w and T2w 4D-MR images in the in-plane and cross-plane directions, respectively. (f) PBM of the original 4D-MR and reconstructed UQ T1w and T2w 4D-MR images. *: P-value < 0.05; **: P-value < 0.001; 4D-MRI: four-dimensional magnetic resonance imaging; AP:

376 anterior-posterior; CNR: contrast-to-noise ratio; FWHM: full width at half maximum;

377 ML: mid-lateral; PMB: perceptual blur metric; ROI: region of interest; SI: superior-

378 inferior; T1w: T1-weighted; T2w: T2-weighted; UQ: ultra-quality.

379

380 **3.3 Statistical Results**

381   UQ T1w and T2w 4D-MRI were obtained on 27 patients who had both 4D-MRI

382 and 3D MRI scans, and ROI motion amplitude was measured on all of them. The results

383 of the statistical analysis of the mean motion error are shown as box plots in **Figure 4(a,**

384 **b)**. The relative ROI motion errors of UQ T1w 4D-MRI in the SI, AP, and ML directions

385 were 0.80 ± 0.36, 0.50 ± 0.36, and 0.50 ± 0.39 mm, respectively. The relative ROI

386 motion errors of UQ T2w 4D-MRI in the SI, AP, and ML directions were 0.78 ± 0.42,

387 0.51 ± 0.36, and 0.52 ± 0.43 mm, respectively. For both contrasts, relative ROI motion

388 errors were 0.79 ± 0.65, 0.50 ± 0.55, and 0.51 ± 0.58 mm in the SI, AP, and ML

389 directions. The relative ROI motion errors were < 1 mm in all directions. The images

390 of 19 of these 27 patients contained visible solid tumors, and CNR was measured only

391 in these images. The results of statistical analysis of the tumor CNR in different MR

392 images are shown as box plots in **Figure 4(c)**. The CNR increased from 7.25 ± 4.89 in

393 the original 4D-MR images to 7.86 ± 5.37 and 18.86 ± 15.81 in the UQ T1w and T2w

394 4D-MR images, respectively. Plots of the lung–liver edge FWHM in the in-plane and

395 cross-plane directions are displayed in **Figure 4(d)** and **Figure 4(e)**, respectively. The

396 lung–liver edge FWHM in the in-plane direction was reduced from 8.22 ± 3.17 mm in

397 the original 4D-MR images to 4.51 ± 1.98 mm and 3.65 ± 1.66 mm in the UQ T1w and

398   T2w 4D-MR images, respectively. In the cross-plane direction, the lung–liver edge

399   FWHM was reduced from 8.79 ± 2.78 mm in the original 4D-MR images to 7.27 ± 2.71

400   mm and 5.04 ± 1.67 mm in the UQ T1w and T2w 4D-MR images, respectively. The

401   PBM results of different 4D-MR images are shown in **Figure 4(f)**. The PBM in the

402   original 4D-MRI was 0.68 ± 0.07, and this value decreased to 0.38 ± 0.01 and $0.40 \pm$

403   0.01 in the UQ T1w and T2w 4D-MR images, respectively.

404

405   **4. Discussion**

406   In this paper, we report the initial results of UQ 4D-MRI using a DDEM based on

407   a commercially available 4D-MRI sequence. The registration performance of DDEM

408   outperformed those of VoxelMorph (NCC supervised), VoxelMorph (EPE supervised),

409   and the pTV algorithm, and the reconstructed UQ 4D-MR images showed significantly

410   improved image quality compared with that of commercial 4D-MRI and yielded

411   accurate tumor motion measurements with a fast processing time.

412   The use of dual supervision is believed to explain the superior performance of

413   DDEM over VoxelMorph (NCC supervised), VoxelMorph (EPE supervised), and the

414   pTV algorithm. Medical image registration has been a hot research topic for decades,

415   and numerous methods have been proposed. Despite huge successes, low-quality image

416   registration remains a big challenge, and the accuracy of both iterative and deep

417   learning methods worsens as the down-sampling factor increases[36]. Guidance from

418   reference DVFs can encourage the convergence and improve the performance of

419   DDEM., even if the original 4D-MR images are noisy and blurred. On the other hand,

420 guidance from image similarity can further fine-tune the registration and help surpass

421 the reference DVFs. Fan et al.[28] demonstrated a similar improvement in registration

422 accuracy with dual supervision, although their model was patch-based and evaluated

423 using high-quality brain MR images. We extended our method to predict the

424 deformation of the whole ROI and 4D-MR images with respiratory motion. Preparing

425 reference DVFs can be time-consuming and may limit the application of dual

426 supervision[24-26]. However, the reference DVFs were only needed during model training

427 and dual supervision did not introduce any additional latency in inference, as shown in

428 **Table 2**.

429   The reconstructed UQ 4D-MR images generated via DDEM exhibited significant

430 improvements in image quality, including tumor CNR and image texture, compared

431 with the original 4D-MR images. In particular, the lung–liver edges were sharper, and

432 blurring artifacts were considerably decreased. The tumor motion trajectories derived

433 from UQ 4D-MR images were comparable to those derived from the original 4D-MR

434 images, with a mean error < 1 mm in all directions, suggesting that our method

435 accurately reflects tumor motion. Also, the motion trajectories show no significant

436 difference between UQ T1w and T2w 4D-MRI, which is expected since they were

437 derived from the same DVF. However, potential errors might exist in pre-processing,

438 such as inaccurate alignment in frame selection. The consistent tumor motion

439 trajectories in both UQ 4D-MR images can be a quality assurance of the entire workflow.

440 The image quality of reconstructed UQ 4D-MRI is inherited from 3D MRI, and so are

441 the artifacts. For example, the T1w 3D MRI was acquired under free-breathing and

volume-averaging artifacts present, especially at the lung-liver interface. The T2w 3D

MRI was acquired under breath-holding with multiple concatenations (typically 4~5),

resulting in the bright or dark slabs. The reconstructed UQ 4D-MRI also shows these

artifacts. However, these artifacts do not affect the accuracy of DDEM and UQ 4D-

MRI reconstruction, since registration was only conducted between the original 4D-

MRI frames.

We have shown that our UQ 4D-MRI method has major advantages over current

retrospective 4D-MRI methods, which rely on sorting algorithms and are thus

vulnerable to irregular breathing and can cause stitching artifacts or missing slices.

Furthermore, the spatial resolution of existing methods is often compromised due to the

time efficiency and data sufficiency requirements of retrospective 4D-MRI, and the

acquisition times are relatively long. In contrast, our method uses 3D MR images as

prior knowledge. The resulting UQ 4D-MR images inherit quality from these prior

images and thus can achieve a comparable level of image quality, which is indicated by

smooth and complete organ surfaces and fine voxel sizes. In addition, apart from image

acquisition, our method generates UQ 4D-MR images at a speed of 60 ms per

volumetric frame, making it highly applicable in the clinic.G

Our UQ 4D-MRI method also has advantages over current prospective 4D-MRI

methods, which often produce images with compromised quality, have limited image

contrast choices, and are sensitive to field inhomogeneity. As noted above, the quality

of images generated using our method is comparable to that of the prior 3D MR images,

which can be acquired via sequences robust to field inhomogeneity, such as fast spin

464 echo. Our method also provides versatile image contrast choices. Although only T1w

465 and T2w 4D-MR images were reconstructed in this study, our method can be further

466 extended to multiple types of image contrast if corresponding 3D MR images are

467 provided.

468   Our method can also be used to obtain accurate 3D tumor motion trajectories,

469 whereas other studies investigating prior image-based time-resolved 4D-MRI have only

470 evaluated tumor motion trajectories on 2D images or projections. For example, Harris

471 et al. modeled a patient's basic deformation patterns using principal component analysis

472 (PCA) and calculated the coefficients for those patterns based on a single 2-dimensional

473 (2D) cine MRI[37], multiple 2D cine MRI[38], or on-board kV projections[39]. The

474 deformation was then applied to a prior MR image to generate real-time volumetric

475 cine MRI for lung tumor patients. Pham et al. [40] developed a similar method but used a

476 neural network to predict pattern coefficients. In that study, the high contrast between

477 the tumor and normal tissue in the lungs made it relatively easy to capture and model

478 tumor motion. In contrast, we focused on liver tumors when developing our method,

479 which are more challenging due to the poor contrast. Additionally, both of their ground

480 truth motion trajectories were obtained from one or multiple 2D images and thus may

481 not reflect accurate 3D tumor motion, resulting in misleading 3D image deformation.

482 In contrast, our method directly tracks tumor motion on 3D images and yields more

483 reliable results. Finally, the deformation reported in earlier studies involved a

484 combination of basic patterns, and small motions may have been omitted during motion

485 modeling. Our method uses DIR for deformation estimation, which theoretically can

486   capture any motion.

487   Our UQ method can be used to facilitate the application of 4D-MRI for clinical

488   purposes, including target volume delineation and on-board treatment guidance. Zhang

489   et al. showed that a fusion of multisource MRI could significantly improve the tumor

490   CNR compared with a single type of contrast[41], leading to improved inter-observer

491   consistency during gross tumor volume delineation[42]. Due to monetary and temporal

492   limitations, it may be impractical to require patients to undergo multiple 4D-MRI scans.

493   Our method enables patients to undergo multiple 3D MRI scans and obtain UQ 4D-MR

494   images with various contrasts. Current MRI-based on-board treatment guidance relies

495   on 2D cine MRI with orthogonal views, which can only provide information about

496   tumor motion on a couple of projections[43]. In contrast, our method enables real-time

497   4D-MRI if the temporal resolution of the original 4D-MRI is sufficient, thus providing

498   more accurate information for treatment monitoring and tracking.

499   One limitation of our study is the absence of functional images. DWI and dynamic

500   contrast-enhanced (DCE) images provide additional information beyond anatomical

501   images, which can potentially facilitate the localization of liver tumors[44] and

502   metastases[45]. However, this study focused only on T1w and T2w images to demonstrate

503   the feasibility of our method. In future research, we will enroll additional patients with

504   functional MR image data, including DWI and DCE images, to further verify the

505   generalizability of our method. Another limitation is the temporal resolution of UQ 4D-

506   MRI. Currently, the acquisition time of conventional 4D-MRI is 0.69 s per frame to

507   achieve good image quality, which yields around six frames per typical respiratory

508   cycle (~4 s). Some studies have demonstrated the feasibility of DVF estimation using

509   highly undersampled images[36]. In the future, we will further reduce the acquisition time

510   of the original commercial 4D-MRI scans to improve the temporal resolution. Finally,

511   the generalizability of our method needs further evaluation. We did not introduce any

512   specially designed types of processing to the dataset, and we expect that our method

513   will be robust to other patient cohorts and commercial MRI sequences. We will enroll

514   patients at other hospitals that use different scanning protocols to further evaluate the

515   generalizability of our method.

516

5. Conclusion

518   This study developed a novel DDEM for fast UQ 4D-MRI reconstruction based on

519   a commercially available 4D-MRI sequence. Compared with the original 4D-MR

520   images, the reconstructed UQ 4D-MR images provided versatile image contrast,

521   significantly improved image quality, and accurate tumor motion trajectories within a

522   short processing time. This method overcomes the limitations of current retrospective

523   and prospective 4D-MRI methods and shows great promise as a means of expanding

524   the clinical implementation of 4D-MRI for liver cancer motion management during RT.

525

526 **Reference:**

527   1.   Sung H, Ferlay J, Siegel RL, et al. Global cancer statistics 2020: GLOBOCAN estimates of
528 incidence and mortality worldwide for 36 cancers in 185 countries. *CA Cancer J Clin*.
529 2021;71(3):209-249. doi:https://doi.org/10.3322/caac.21660

530   2.   Chen CP. Role of radiotherapy in the treatment of hepatocellular carcinoma. *J Clin Transl*
531 *Hepatol*. 2019;7(2):183-190. doi:10.14218/JCTH.2018.00060

532   3.   Gerum S, Heinz C, Belka C, et al. Stereotactic body radiation therapy (SBRT) in patients with
533 hepatocellular carcinoma and oligometastatic liver disease. *Radiation Oncology*. 2018/05/29
534 2018;13(1):100. doi:10.1186/s13014-018-1048-4

535   4.   Rim CH, Kim HJ, Seong J. Clinical feasibility and efficacy of stereotactic body radiotherapy for
536 hepatocellular carcinoma: a systematic review and meta-analysis of observational studies.
537 *Radiother Oncol*. 2019/02/01/ 2019;131:135-144.
538 doi:https://doi.org/10.1016/j.radonc.2018.12.005

539   5.   Murray LJ, Dawson LA. Advances in stereotactic body radiation therapy for hepatocellular
540 carcinoma. *Semin Radiat Oncol*. 2017/07/01/ 2017;27(3):247-255.
541 doi:https://doi.org/10.1016/j.semradonc.2017.02.002

542   6.   Scorsetti M, Comito T, Cozzi L, et al. The challenge of inoperable hepatocellular carcinoma
543 (HCC): results of a single-institutional experience on stereotactic body radiation therapy (SBRT). *J*
544 *Cancer Res Clin Oncol*. 2015/07/01 2015;141(7):1301-1309. doi:10.1007/s00432-015-1929-y

545   7.   Keall PJ, Mageras GS, Balter JM, et al. The management of respiratory motion in radiation
546 oncology report of AAPM Task Group 76. *Med Phys*. Oct 2006;33(10):3874-3900.
547 doi:10.1118/1.2349696

548   8.   Hof H, Rhein B, Haering P, Kopp-Schneider A, Debus J, Herfarth K. 4D-CT-based target
549 volume definition in stereotactic radiotherapy of lung tumours: comparison with a conventional
550 technique using individual margins. *Radiother Oncol*. 2009;93(3):419-423.
551 doi:https://doi.org/10.1016/j.radonc.2009.08.040

552   9.   Wang L, Hayes S, Paskalev K, et al. Dosimetric comparison of stereotactic body radiotherapy
553 using 4D CT and multiphase CT images for treatment planning of lung cancer: evaluation of the
554 impact on daily dose coverage. *Radiother Oncol*. 2009;91(3):314-324.
555 doi:https://doi.org/10.1016/j.radonc.2008.11.018

556   10. Zhao L, Sandison GA, Farr JB, Hsi WC, Li XA. Dosimetric impact of intrafraction motion for
557 compensator-based proton therapy of lung cancer. *Phys Med Biol*. Jun 21 2008;53(12):3343.
558 doi:10.1088/0031-9155/53/12/019

559   11. Underberg RW, Lagerwaard FJ, Cuijpers JP, Slotman BJ, De Koste JRVS, Senan S. Four-
560 dimensional CT scans for treatment planning in stereotactic radiotherapy for stage I lung cancer.
561 *Int J Radiat Oncol Biol Phys*. Nov 15 2004;60(4):1283-1290. doi:10.1016/j.ijrobp.2004.07.665

562   12. Li T, Schreibmann E, Thorndyke B, et al. Radiation dose reduction in four-dimensional
563 computed tomography. *Med Phys*. 2005;32(12):3650-3660.
564 doi:https://doi.org/10.1118/1.2122567

565   13. Stemkens B, Paulson ES, Tijssen RH. Nuts and bolts of 4D-MRI for radiotherapy. *Phys Med*
566 *Biol*. 2018;63(21):21TR01. doi:10.1088/1361-6560/aae56d

567   14. Yang J, Cai J, Wang H, et al. Is diaphragm motion a good surrogate for liver tumor motion?
568 *Int J Radiat Oncol Biol Phys*. Nov 15 2014;90(4):952-8. doi:10.1016/j.ijrobp.2014.07.028

569　15.　Yang J, Cai J, Wang H, et al. Four-dimensional magnetic resonance imaging using axial body
570　area as respiratory surrogate: initial patient results. *Int J Radiat Oncol Biol Phys*. 2014;88(4):907-
571　912. doi:https://doi.org/10.1016/j.ijrobp.2013.11.245
572　16.　Liu Y, Yin F-F, Chen N-k, Chu M-L, Cai J. Four dimensional magnetic resonance imaging with
573　retrospective　k-space　reordering:　A　feasibility　study.　2015;42(2):534-541.
574　doi:https://doi.org/10.1118/1.4905044
575　17.　Keijnemans K, Borman PTS, van Lier A, Verhoeff JJC, Raaymakers BW, Fast MF. Simultaneous
576　multi-slice　accelerated　4D-MRI　for　radiotherapy　guidance. *Phys　Med　Biol*. Apr　28
577　2021;66(9)doi:10.1088/1361-6560/abf591
578　18.　Liu Y, Yin FF, Czito BG, Bashir MR, Cai J. T2-weighted four dimensional magnetic resonance
579　imaging　with　result-driven　phase　sorting. *Med　Phys*. Aug　2015;42(8):4460-71.
580　doi:10.1118/1.4923168
581　19.　Liu Y, Zhong X, Czito BG, et al. Four-dimensional diffusion-weighted MR imaging (4D-DWI):
582　a feasibility study. *Med Phys*. 2017;44(2):397-406. doi:https://doi.org/10.1002/mp.12037
583　20.　Li T, Cui D, Hui ES, Cai J. Time-resolved magnetic resonance fingerprinting for radiotherapy
584　motion management. *Med Phys*. Dec 2020;47(12):6286-6293. doi:10.1002/mp.14513
585　21.　Yuan J, Wong OL, Zhou Y, Chueng KY, Yu SK. A fast volumetric 4D-MRI with sub-second
586　frame rate for abdominal motion monitoring and characterization in MRI-guided radiotherapy.
587　*Quant Imaging Med Surg*. 2019;9(7):1303. doi:10.21037/qims.2019.06.23
588　22.　Li G, Wei J, Olek D, et al. Direct comparison of respiration-correlated four-dimensional
589　magnetic resonance imaging reconstructed using concurrent internal navigator and external
590　bellows. *International　Journal　of　Radiation　Oncology*Biology*Physics*.　2017/03/01/
591　2017;97(3):596-605. doi:https://doi.org/10.1016/j.ijrobp.2016.11.004
592　23.　Block KT, Chandarana H, Fatterpekar G, et al. Improving the robustness of clinical T1-
593　weighted MRI using radial VIBE. *Magnetom Flash*. 2013;5:6-11.
594　24.　Fu Y, Lei Y, Wang T, Curran WJ, Liu T, Yang X. Deep learning in medical image registration: a
595　review. *Phys Med Biol*. Oct 22 2020;65(20):20TR01. doi:10.1088/1361-6560/ab843e
596　25.　Haskins G, Kruger U, Yan P. Deep learning in medical image registration: a survey. *Machine
597　Vision and Applications*. 2020;31(1):8. doi:https://doi.org/10.1007/s00138-020-01060-x
598　26.　Xiao H, Teng X, Liu C, et al. A review of deep learning-based three-dimensional medical
599　image registration methods. *Quant Imaging Med Surg*. 2021;
600　27.　Mengler L, Khmelinskii A, Diedenhofen M, et al. Brain maturation of the adolescent rat cortex
601　and striatum: changes in volume and myelination. *Neuroimage*. 2014/01/01/ 2014;84:35-44.
602　doi:https://doi.org/10.1016/j.neuroimage.2013.08.034
603　28.　Fan JF, Cao XH, Yap EA, Shen DG. BIRNet: Brain image registration using dual-supervised fully
604　convolutional networks. *Med Image Anal*. May 2019;54:193-206. doi:10.1016/j.media.2019.03.006
605　29.　Vishnevskiy V, Gass T, Szekely G, Tanner C, Goksel O. Isotropic total variation regularization
606　of displacements in parametric image registration. *IEEE Trans Med Imaging*. Feb 2016;36(2):385-
607　395. doi:10.1109/TMI.2016.2610583
608　30.　Castillo　R, Castillo　E, Guerra　R, et al. A framework for evaluation of deformable image
609　registration spatial accuracy using large landmark point sets. *Phys Med Biol*. 2009;54(7):1849.
610　doi:http://dx.doi.org/10.1088/0031-9155/54/7/001
611　31.　Castillo R, Castillo E, Fuentes D, et al. A reference dataset for deformable image registration
612　spatial　accuracy　evaluation　using　the　COPDgene　study　archive. *Phys　Med　Biol*. May　7

2013;58(9):2861-77. doi:10.1088/0031-9155/58/9/2861

32. Fan J, Cao X, Yap P-T, Shen D. BIRNet: Brain image registration using dual-supervised fully convolutional networks. *Med Image Anal*. 2019;54:193-206. doi:https://doi.org/10.1016/j.media.2019.03.006

33. Balakrishnan G, Zhao A, Sabuncu MR, Guttag J, Dalca AV. VoxelMorph: a learning framework for deformable medical image registration. *IEEE Trans Med Imaging*. Feb 4 2019;doi:10.1109/TMI.2019.2897538

34. Crete F, Dolmiere T, Ladret P, Nicolas M. The blur effect: perception and estimation with a new no-reference perceptual blur metric. International Society for Optics and Photonics; 2007:64920I.

35. Ahmad R, Ding Y, Simonetti OP. Edge sharpness assessment by parametric modeling: application to magnetic resonance imaging. *Concepts Magn Reson Part A Bridg Educ Res*. May 1 2015;44(3):138-149. doi:10.1002/cmr.a.21339

36. Terpstra ML, Maspero M, D'Agata F, et al. Deep learning-based image reconstruction and motion estimation from undersampled radial k-space for real-time MRI-guided radiotherapy. *Phys Med Biol*. 2020;65(15):155015. doi:10.1088/1361-6560/ab9358

37. Harris W, Ren L, Cai J, Zhang Y, Chang Z, Yin F-F. A technique for generating volumetric cine-magnetic resonance imaging. *International Journal of Radiation Oncology*Biology*Physics*. 2016/06/01 2016;95(2):844-853. doi:https://doi.org/10.1016/j.ijrobp.2016.02.011

38. Harris W, Yin F-F, Cai J, Ren L. Volumetric cine magnetic resonance imaging (VC-MRI) using motion modeling, free-form deformation and multi-slice undersampled 2D cine MRI reconstructed with spatio-temporal low-rank decomposition. *Quant Imaging Med Surg*. 2020;10(2):432-450. doi:10.21037/qims.2019.12.10

39. Harris W, Wang C, Yin F-F, Cai J, Ren L. A novel method to generate on-board 4D MRI using prior 4D MRI and on-board kV projections from a conventional LINAC for target localization in liver SBRT. *Med Phys*. 2018;45(7):3238-3245. doi:https://doi.org/10.1002/mp.12998

40. Pham J, Harris W, Sun W, Yang Z, Yin FF, Ren L. Predicting real-time 3D deformation field maps (DFM) based on volumetric cine MRI (VC-MRI) and artificial neural networks for on-board 4D target tracking: a feasibility study. *Phys Med Biol*. Aug 21 2019;64(16):165016. doi:10.1088/1361-6560/ab359a

41. Zhang L, Yin F-F, Moore B, Han S, Cai J. A multisource adaptive magnetic resonance image fusion technique for versatile contrast magnetic resonance imaging. Original Article. *Cancer Translational Medicine*. May 1, 2018 2018;4(3):65-69. doi:10.4103/ctm.ctm_21_18

42. Zhang J, Srivastava S, Wang C, et al. Clinical evaluation of 4D MRI in the delineation of gross and internal tumor volumes in comparison with 4DCT. *J Appl Clin Med Phys*. 2019;20(9):51-60. doi:https://doi.org/10.1002/acm2.12699

43. Wang C, Yin F-F. 4D-MRI in radiotherapy. IntechOpen; 2019.

44. Kim J-E, Kim SH, Lee SJ, Rhim H. Hypervascular hepatocellular carcinoma 1 cm or smaller in patients with chronic liver disease: characterization with gadoxetic acid–enhanced MRI that includes diffusion-weighted imaging. *American Journal of Roentgenology*. 2011/06/01 2011;196(6):W758-W765. doi:10.2214/AJR.10.4394

45. Colagrande S, Castellani A, Nardi C, Lorini C, Calistri L, Filippone A. The role of diffusion-weighted imaging in the detection of hepatic metastases from colorectal cancer: A comparison with unenhanced and Gd-EOB-DTPA enhanced MRI. *Eur J Radiol*. 2016/05/01 2016;85(5):1027-

657   1034. doi:https://doi.org/10.1016/j.ejrad.2016.02.011

658